

3D LiDAR Aided GNSS Real-time Kinematic Positioning

Weisong Wen and Li-Ta Hsu

Interdisciplinary Division of Aeronautical and Aviation Engineering, The Hong Kong Polytechnic University

BIOGRAPHY

Weisong Wen received a Ph.D. degree in Mechanical Engineering from The Hong Kong Polytechnic University (PolyU), in Nov 2020. He was also a visiting Ph.D. student with the Faculty of Engineering, University California, Berkeley (UC Berkeley) in 2018. In 2020, he won the Best Presentation Award from the Institute of Navigation (ION), and the First Prize in Hong Kong Section in Qianhai-Guangdong-Macao Youth Innovation and Entrepreneurship Competition, 2019. Before joining PolyU as a Research Assistant Professor in April 2021, he was a senior research fellow at PolyU. His research interests include GNSS positioning, SLAM, and collaborative positioning in challenging environments autonomous driving vehicles, and unmanned aerial vehicles.

Li-Ta Hsu received the B.S. and Ph.D. degrees in aeronautics and astronautics from National Cheng Kung University, Taiwan, in 2007 and 2013, respectively. He is currently an assistant professor with the Interdisciplinary Division of Aeronautical and Aviation Engineering, The Hong Kong Polytechnic University, before he served as a post-doctoral researcher in the Institute of Industrial Science at the University of Tokyo, Japan. In 2012, he was a visiting scholar at University College London, the U.K. His research interests include GNSS positioning in challenging environments and localization for pedestrian, autonomous driving vehicle, and unmanned aerial vehicle

ABSTRACT

Global navigation satellite system real-time kinematic (GNSS-RTK) positioning is an indispensable source for providing absolute positioning for autonomous driving vehicles (ADV), due to its high accuracy when a fixed solution is achieved. Satisfactory accuracy can be obtained in open areas. However, the performance of GNSS-RTK can be significantly degraded by signal reflections from buildings, causing multipath effects and non-line-of-sight (NLOS) receptions. To fill this gap, this paper proposed a novel method to exclude the potential GNSS NLOS receptions, aided by the local environment description generated with 3D LiDAR and inertial sensor, to further improve the GNSS-RTK. The local environment description, the 3D point cloud map, is built via LiDAR/inertial integration using factor graph optimization. Then the potential GNSS NLOS receptions are detected and remove using the 3D point cloud maps before the GNSS-RTK positioning. Finally, the improved GNSS-RTK positioning is adopted to correct the drift of the 3D point cloud map derived from LiDAR/inertial integration. The effectiveness of the proposed method is verified through a challenging dataset collected in urban canyons of Hong Kong using the automobile-level low-cost GNSS receiver.

1. INTRODUCTION

The global navigation satellite system real-time kinematic (GNSS-RTK) is widely used for high precision aerial mapping [1] and positioning for level-4 fully autonomous driving vehicles [2]. Typically, the GNSS-RTK positioning involves two steps: (1) The float solution is estimated based on the received GNSS measurements. (2) Then the integer ambiguity is resolved using least-squares algorithms (e.g LAMBDA [3]) based on the derived float solution as an initial guess. Centimeter-level positioning accuracy can be achieved based on the double-differential carrier and code measurements in the open area when the fixed solution is achieved. Unfortunately, the accuracy of GNSS-RTK is significantly degraded in urban canyons due to the none-line-of-sight (NLOS) and multipath receptions caused by GNSS signal reflection and blockage from surrounding buildings. In practice, the significantly degraded GNSS-RTK positioning accuracy in urban canyons is mainly led by the occurrence of GNSS NLOS receptions. Part of the received GNSS signals is significantly polluted involving large noise. According to our previous research in [4], the majority of the received GNSS signals can be multipath or NLOS receptions in highly urbanized areas. Therefore, the accuracy of the float solution estimation based on the differential carrier and code measurements is degraded, making the ambiguity resolution hard to get a fixed solution.

Numerous researches [5-7] were studied to improve the GNSS-RTK positioning performance in urban canyons in the past decades. The work in [6] proposed to employ multiple antennas to improve the robustness of GNSS-RTK against the outlier measurements. However, the method relied on the percentage of the polluted GNSS signals (multipath or NLOS receptions). The recent work in [5] proposed to improve the GNSS-RTK in urban canyons by excluding polluted GNSS signals with the help of 3D building models. The increased fixed rate was obtained after selecting the healthy line-of-sight (LOS) measurements. However, the satellite exclusion relies on the availability of accurate 3D building models and the initial guess of the GNSS receiver's position. Another research stream was to employ the additional sensors via sensor fusion. The integration of the GNSS-RTK and inertial measurement unit (IMU) was widely studied due to their complementariness. The work in [8] showed that with the help of better signal availability, high-grade dual-frequency multi-GNSS RTK can achieve correct integer fixing rates of 76.7% on a 1-hour drive along with a typical urban scene. However, the overall performance relies heavily on the cost of the IMU sensor during the GNSS outage [9]. The work in [10, 11] proposed to tightly integrate the GNSS-RTK with the vision measurements in GNSS-challenged environments. Unfortunately, the vision measurements are sensitive to the illumination conditions and density of dynamic objects [12]. Moreover, the recovery of the scale of the visual measurement relies heavily on the quality of the GNSS measurements. Instead of using the visual measurements, our previous works in [4, 13-15] proposed to continuously improve the GNSS single point positioning (SPP) using in urban canyons 3D LiDAR sensor which is robust to illumination conditions. The 3D point clouds from the 3D LiDAR sensor are employed to describe the surrounding environment to further exclude [4] or correct GNSS NLOS receptions [13]. The latest work in [16] combines both the GNSS NLOS correction and re-modeling to improve the urban GNSS SPP based on the incrementally built environmental description (3D point cloud maps). However, only the code measurements are applied and the potential of the carrier-phase measurements is not explored.

Inspired by our previous works on 3D LiDAR aided GNSS SPP [4, 13], in this paper, we proposed to improve the GNSS-RTK positioning in urban canyons using a 3D LiDAR sensor by essentially tackling the listed problem of GNSS-RTK due to the signal reflections and the blockage. Firstly, LiDAR/inertial odometry (LIO), which loosely integrates LiDAR and the IMU measurements using factor graph optimization (FGO) based on our recent work in [17], is performed to estimate the relative motion between two epochs and generate the 3D point cloud map (PCM), so-called the local environmental description. Secondly, the potential GNSS NLOS satellites are detected and excluded with the help of the generated point cloud map based on our previous work in [16]. Therefore, the problem of poor GNSS measurement quality is alleviated by excluding the potential GNSS NLOS receptions. Secondly, the float solution can be estimated based on the survived GNSS satellite measurements. Then the LAMBDA algorithm is applied to perform the ambiguity resolution. Finally, the estimated fixed GNSS-RTK positioning solution is used to fuse with the LIO to further correct the drift of the 3D point clouds. In short, the proposed method effectively combines the complementariness of LIO (locally accurate in a short period and provides environmental description for GNSSNLOS detection) and GNSS-RTK (free of drift with globally referenced positioning but affected by the GNSS NLOS). The contributions of this paper are listed as follows:

- (1) This paper proposed to use the LiDAR/inertial integration to detect and exclude the GNSS NLOS to further improve the GNSS-RTK positioning. To the best of the author's knowledge, this is the first work that enables the GNSS NLOS exclusion for GNSS-RTK positioning using LiDAR/inertial integration.
- (2) This paper proposed to adopt the improved GNSS-RTK positioning to correct the drift of the 3D point clouds, and therefore, improve the overall positioning accuracy.
- (3) This paper evaluates the performance of the proposed method using the dataset collected using a low-cost GNSS receiver.

The remainder of this paper is organized as follows. An overview of the proposed method is given in Section 2. The generation of the local environmental description is elaborated in Section 3. In Section 4, the proposed NLOS detection and GNSS-RTK positioning are presented. An experiment is performed to evaluate the effectiveness of the proposed method using a dataset collected in urban canyons of Hong Kong in Section 5. Finally, conclusions are drawn, and further work is presented in Section 6.

2. OVERVIEW OF THE PROPOSED METHOD

An overview of the method proposed in this paper is shown in Fig. 1. The system consists of two parts: (1) the real-time environment description generation based on clouds from 3D LiDAR and an IMU, together with the correction from the GNSS-RTK solution. (2) the GNSS NLOS detection and exclusion based on the real-time environment description, and the GNSS-RTK positioning based on surviving satellites. In this paper, matrices are denoted as uppercase with bold letters. Vectors are denoted as lowercase with bold letters. Variable scalars are denoted as lowercase italic letters. Constant scalars are denoted as lowercase letters. Meanwhile, the state of the GNSS receiver and the position of satellites are all expressed in the east, north, and up coordinate.

To make the proposed pipeline clear, the following major notations are defined and followed by the rest of the paper.

- The pseudorange measurement received from a satellite s at a given epoch k is expressed as $\rho_{r,k}^s$. The subscript r and k denote the GNSS receiver and the time index, respectively. The superscript s denotes the index of the satellite.
- The carrier-phase measurement received from a satellite s at a given epoch k is expressed as $\psi_{r,k}^s$.
- The variable expressed in the earth-centered, earth-fixed (ECEF) frame or east, north, and up (ENU) frames is denoted by superscripts “ G ”, “ L ”. For example, the transformation from the ENU and the ECEF frame is defined as $\mathbf{T}_L^G = [\mathbf{R}_L^G \quad \mathbf{t}_L^G]$, where the \mathbf{R}_L^G and the \mathbf{t}_L^G denote the rotation and translation, respectively.
- The body frames of AHRS, LiDAR, and GNSS receiver are denoted by superscripts “ BI ”, “ BL ”, and “ BR ”. For example, \mathbf{P}_k^{BL} denotes a frame of 3D point clouds from 3D LiDAR at epoch k .
- The extrinsic parameters between the GNSS receiver and the 3D LiDAR are denoted as $\mathbf{T}_{BL}^{BR} = [\mathbf{R}_{BL}^{BR} \quad \mathbf{t}_{BL}^{BR}]$. The extrinsic parameters between the IMU and the 3D LiDAR are denoted as $\mathbf{T}_{BL}^{BI} = [\mathbf{R}_{BL}^{BI} \quad \mathbf{t}_{BL}^{BI}]$.
- The position of the satellite s at a given epoch k is expressed as $\mathbf{p}_k^{G,s} = (p_{k,x}^{G,s}, p_{k,y}^{G,s}, p_{k,z}^{G,s})^T$.
- The position of the GNSS receiver at a given epoch k in the ECEF and ENU frames are expressed as $\mathbf{p}_{r,k}^G = (p_{r,k,x}^G, p_{r,k,y}^G, p_{r,k,z}^G)^T$, $\mathbf{p}_{r,k}^L = (p_{r,k,x}^L, p_{r,k,y}^L, p_{r,k,z}^L)^T$. The rotation in the ENU frame is denoted as $\mathbf{R}_{r,k}^L = (\alpha_{r,k,x}^L, \beta_{r,k,y}^L, \gamma_{r,k,z}^L)^T$.
- The clock bias of the GNSS receiver at a given epoch k is expressed as $\delta_{r,k}$, that with the unit in meters. $\delta_{r,k}^s$ denotes the satellite clock bias by meters.

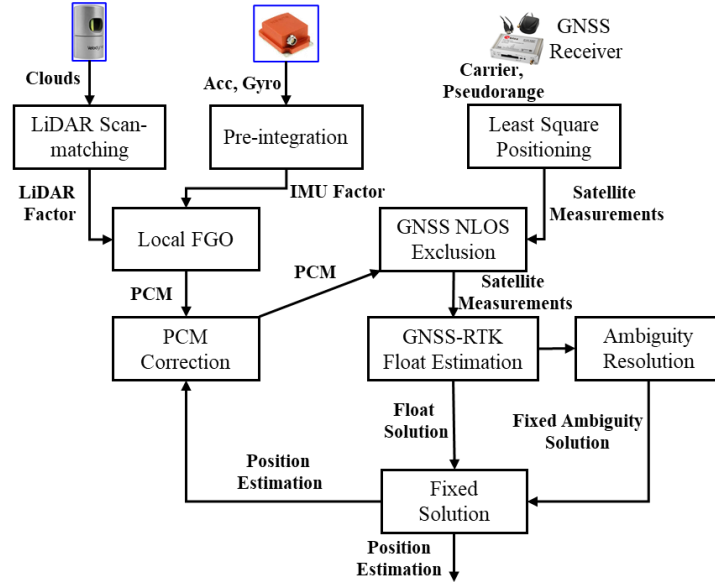


Fig. 1. Overview of the proposed method. The inputs are the raw measurements from IMU, 3D LiDAR, and GNSS receiver. The output is the state estimation of the GNSS receiver.

3. LOCAL ENVIRONMENTAL DESCRIPTION GENERATION

This section presents the methodology for the local environmental description generation based on LiDAR/inertial sensor, together with the correction from the GNSS-RTK. The LiDAR/inertial integration is firstly adopted to generate the 3D point cloud map using a local FGO (see Fig. 1). Then the 3D point cloud map is employed to detect the GNSS NLOS receptions. However, the LiDAR/inertial integration is subjected to drift over time. Therefore, the improved GNSS-RTK positioning result is employed to correct the 3D point cloud map by integrating the GNSS-RTK with the LIO using a global FGO (see Fig. 1). Be noted that the PCM is denoted in the ENU frame. Meanwhile, the extrinsic parameters ($\mathbf{T}_{BL}^{L(0)}$) between the ENU frame and the original of the LiDAR frame $BL^{(0)}$ is calibrated using the first several fixed solutions from GNSS-RTK [18].

3.1 Solving Local FGO

The LiDAR/inertial integration is based on our previous work in [17]. The combined objective function can be formulated as follow to optimize the state set $\mathbf{X}^{BL^{(0)}}$ inside the sliding window:

$$\mathbf{X}^{BL(0)*} = \min_{\mathbf{X}^{BL(0)}} \frac{1}{2} \left\{ \sum_{k \in \{0, \dots, K\}} \rho \left(\left\| \mathbf{r}_L \left(\mathbf{T}_{BL_k}^{BL(0)}, \mathbf{X}^{BL(0)} \right) \right\|_{\mathbf{C}_{L_k}}^2 \right) + \sum_{k \in \{0, \dots, K-1\}} \rho \left(\left\| \mathbf{r}_B \left(\mathbf{z}_{BI_{k+1}}^{BI_k}, \mathbf{X}^{BL(0)} \right) \right\|_{\mathbf{C}_{BI_{k+1}}^{BI_k}}^2 \right) \right\}, \quad (1)$$

where the $\mathbf{r}_L \left(\mathbf{T}_{BL_k}^{BL(0)}, \mathbf{X}^{BL(0)} \right)$ represents the residuals of LiDAR scan-matching factor, $\mathbf{z}_{BI_{k+1}}^{BI_k}$ and $\mathbf{r}_B \left(\mathbf{z}_{BI_{k+1}}^{BI_k}, \mathbf{X}^{BL(0)} \right)$ represents the measurements and the residuals produced by the IMU pre-integration factor, respectively, $\mathbf{X}^{BL(0)*}$ are the optimal states to be estimated. The \mathbf{C}_{L_k} denotes the covariance matrix of the LiDAR scan-matching factor which is derived based on [17]. The $\mathbf{C}_{BI_{k+1}}^{BI_k}$ denotes the covariance matrix of the IMU pre-integration factor. The $\rho(*)$ denotes the robust loss function and the Cauchy kernel [19] is selected in this paper. Finally, the Ceres solver [20] is used to solve this nonlinear problem and we exploit the Levenberg-Marquardt (L-M) algorithm [21] to iteratively minimize the cost function (1). Therefore, the PCM can be acquired by accumulated the raw 3D point clouds inside the sliding window of local FGO based on the state set $\mathbf{X}^{BL(0)}$, which is denoted as $\mathbf{M}_k^{BL(0)}$.

3.2 LIO/GNSS-RTK Integration using Global FGO

The global FGO integrates the pose estimation from the LIO presented in Section 3.1, and the GNSS-RTK positioning. Similar to the LIO, the state set inside the sliding window is optimized. The k -th state of the IMU frame in the ENU frame can be written as:

$$\mathbf{x}_k^L = [\mathbf{p}_{BI_k}^L, \mathbf{q}_{BI_k}^L], \quad (2)$$

where \mathbf{x}_k^L consists of the position, and rotation in quaternion form in the ENU frame. Therefore, the state set (\mathbf{X}^L) inside a local window of the FGO can be denoted as:

$$\mathbf{X}^L = [\mathbf{x}_0^L, \mathbf{x}_1^L, \dots, \mathbf{x}_K^L], \quad (3)$$

where the K denotes the size of the sliding window of the FGO. Assuming the position estimation from the improved GNSS-RTK is denoted as follows:

$$\mathbf{z}_{r,k}^G = (p_{r,k,x}^G, p_{r,k,y}^G, p_{r,k,z}^G)^T \quad (4)$$

where the $\mathbf{z}_{r,k}^G$ is denoted in the ECEF frame. Therefore, the residual of the $\mathbf{z}_{r,k}^G$ could be derived as follows:

$$\mathbf{r}_{\text{GNSS}}(\mathbf{z}_{r,k}^G, \mathbf{X}^L) = [\mathbf{T}_L^{G^{-1}}(\mathbf{z}_{r,k}^G - \mathbf{t}_L^G) - \mathbf{p}_{BI_k}^L] \quad (5)$$

where the $\mathbf{r}_{\text{GNSS}}(\mathbf{z}_{r,k}^G, \mathbf{X}^L)$ denotes the residual associated with $\mathbf{z}_{r,k}^G$. Based on the LIO, the observation at a given epoch k is $\mathbf{x}_k^{BL(0)}$ and $\mathbf{x}_k^{BL(0)}$ at epoch $k-1$. The residual can be formulated as follows:

$$\mathbf{r}_{\text{LIO}}(\mathbf{x}_{k-1}^{BL(0)}, \mathbf{x}_k^{BL(0)}, \mathbf{x}_{k-1}^L, \mathbf{x}_k^L) = \left[2 \left[\left((\mathbf{P}_1 - \mathbf{P}_2) - (\mathbf{p}_{BI_k}^L - \mathbf{p}_{BI_{k-1}}^L) \right) \otimes \left(\mathbf{q}_{BI_{k-1}}^L \otimes \mathbf{q}_{BI_k}^L \right) \right]_{xyz} \right] \quad (6)$$

$$\text{With } \mathbf{P}_1 = \mathbf{p}_{BL(0)}^L^{-1} \left((\mathbf{R}_{BL}^{BI^{-1}}(\mathbf{p}_{BL_k}^{BL(0)} - \mathbf{t}_{BL}^{BI})) - \mathbf{t}_{BL(0)}^L \right), \mathbf{P}_2 = \mathbf{p}_{BL(0)}^L^{-1} \left((\mathbf{R}_{BL}^{BI^{-1}}(\mathbf{p}_{BL_k}^{BL(0)} - \mathbf{t}_{BL}^{BI})) - \mathbf{t}_{BL(0)}^L \right)$$

where the \mathbf{P}_1 and \mathbf{P}_2 are defined for better representation. Based on the residuals derived above, the combined objective function can be formulated as follow to optimize the state set \mathbf{X}^L inside the sliding window:

$$\mathbf{X}^{L*} = \min_{\mathbf{X}^{BL(0)}} \frac{1}{2} \left\{ \sum_{k \in \{0, \dots, K\}} \rho \left(\left\| \mathbf{r}_{\text{GNSS}}(\mathbf{z}_{r,k}^G, \mathbf{X}^L) \right\|_{\mathbf{C}_{\text{GNSS}}}^2 \right) + \sum_{k \in \{0, \dots, K-1\}} \rho \left(\left\| \mathbf{r}_{\text{LIO}}(\mathbf{x}_{k-1}^{BL(0)}, \mathbf{x}_k^{BL(0)}, \mathbf{x}_{k-1}^L, \mathbf{x}_k^L) \right\|_{\mathbf{C}_{\text{LIO}}}^2 \right) \right\}, \quad (7)$$

where the $\mathbf{r}_{\text{GNSS}}(\mathbf{z}_{r,k}^G, \mathbf{X}^L)$ represents the residuals of the GNSS factor and $\mathbf{r}_{\text{LIO}}(\mathbf{x}_{k-1}^{BL(0)}, \mathbf{x}_k^{BL(0)}, \mathbf{x}_{k-1}^L, \mathbf{x}_k^L)$ represents the residual of the LIO factor, respectively, \mathbf{X}^{L*} are the optimal states to be estimated. The \mathbf{C}_{GNSS} denotes the covariance matrix of the GNSS factor. The \mathbf{C}_{LIO} denotes the covariance matrix of the LIO factor. Similar to the local FGO, the equation (7) is also solved using the Levenberg-Marquardt (L-M) algorithm [21] via Ceres-solver [20]. Therefore, the PCM can be corrected by accumulated the raw 3D point clouds inside the sliding window of global FGO based on the state set \mathbf{X}^L , which is denoted as \mathbf{M}_k^L . Different from

our previous work in [16], the generated PCM is free of drift with the help of the integration of GNSS-RTK positioning. We believe this is also one of the contributions of this paper.

4. NLOS EXCLUSION AND GNSS-RTK POSITIONING

4.1 GNSS NLOS Exclusion Based on PCM

The pseudorange measurement from the GNSS receiver, $\rho_{r,k}^s$, is denoted as follows [22].

$$\rho_{r,k}^s = r_{r,k}^s + c(\delta_{r,k} - \delta_{r,k}^s) + I_{r,k}^s + T_{r,k}^s + \varepsilon_{r,k}^s \quad (8)$$

where $r_{r,k}^s$ is the geometric range between the satellite and the GNSS receiver. $I_{r,k}^s$ represents the ionospheric delay distance; $T_{r,k}^s$ indicates the tropospheric delay distance. $\varepsilon_{r,k}^s$ represents the errors caused by the multipath effects, NLOS receptions, receiver noise, antenna phase-related noise. Meanwhile, the atmosphere effects ($T_{r,k}^s$ and $I_{r,k}^s$) are compensated using the conventional models (Saastamoinen and Klobuchar models, respectively) presented in RTKLIB [23]. Given the PCM in the ENU frame, satellite elevation, and azimuth angles which can be calculated using least squares estimation based on pseudorange measurements, the GNSS NLOS can be detected using the fast searching method proposed in our recent work [16]. The details can be found in [16]. An illustration of the GNSS NLOS receptions detection is shown in Fig. 2.

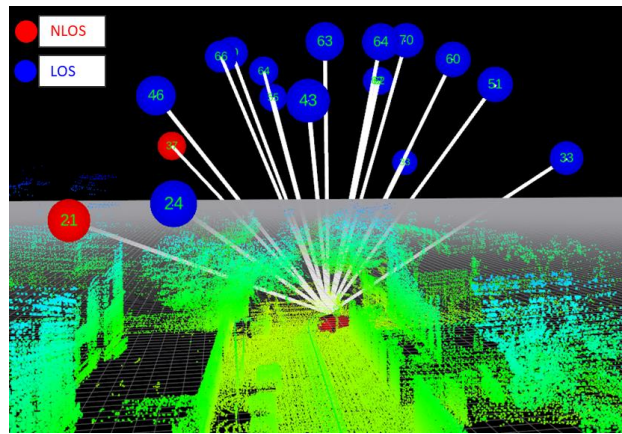


Fig. 2. Demonstration of NLOS detection based on PCM. The red circle denotes the GNSS NLOS satellite. The blue circle denotes the LOS measurements. The number inside the circle denotes the elevation angle of the satellite.

Assume the received satellite set at epoch k is denoted as $\mathbf{SV}_{r,k} = \{\mathbf{SV}_{r,k}^1, \dots, \mathbf{SV}_{r,k}^i, \dots, \mathbf{SV}_{r,k}^N\}$ which involves both the LOS and NLOS satellites. The variable N denotes the number of satellites received at epoch k . The $\mathbf{SV}_{r,k}^i$ denotes the measurements of satellite i . After the GNSS NLOS detection and exclusion, the remaining satellite set is denoted as $\mathbf{SSV}_{r,k} = \{\mathbf{SV}_{r,k}^1, \dots, \mathbf{SV}_{r,k}^i, \dots, \mathbf{SV}_{r,k}^M\}$ where the variable M denotes the number of the remaining satellites.

Based on the survived satellites, the variable $\mathbf{x}_{r,k}^{float*}$ denotes the optimal estimation of the float solution. Therefore, the float solution for GNSS-RTK at the current epoch can be obtained using the conventional least-squares estimation based on our previous work in [24]. After obtaining the float solution of the GNSS-RTK, the ambiguity resolution algorithm is used to estimate the fixed solution. The integer variable should be an integer value when the carrier-phase measurement is free from the noise. This paper makes use of the popular LAMBDA algorithm [25] to solve the integer ambiguity resolution problem and the resolved fixed solution is denoted as $\mathbf{x}_{r,k}^{fix}$. Then the fixed solution is fed to the global FGO to correct the drift in the PCM presented in Section 3.2.

5. EXPERIMENTAL RESULTS AND DISCUSSION

5.1 Experimental Setup

To verify the effectiveness of the proposed method, we collect the dataset in a typical urban scene of Hong Kong. Fig. 3 shows the data collection vehicle installed with multiple sensors. Meanwhile, the tested scene is shown on the right bottom of Fig. 3 which involves tall buildings and trees and is challenging for the GNSS-RTK positioning. In the experiment, a u-blox M8T

GNSS receiver was used to collect raw GPS/BeiDou measurements at a frequency of 1 Hz. A 3D LiDAR sensor (Velodyne 32) was employed to collect raw 3D point clouds at a frequency of 10 Hz. The Xsens Ti-10 IMU was employed to collect data at a frequency of 200 Hz. In addition, the NovAtel SPAN-CPT, a GNSS (GPS, GLONASS, and BeiDou) RTK/INS (fiber-optic gyroscopes, FOG) integrated navigation system was used to provide ground truth of positioning. The gyro bias in-run stability of the FOG is 1 degree per hour, and its random walk is 0.067 degrees per hour. The baseline between the rover and the GNSS base station is about 5 km. All the data were collected and synchronized using a robot operation system (ROS) [26]. The coordinate systems between all the sensors were calibrated before the experiments.

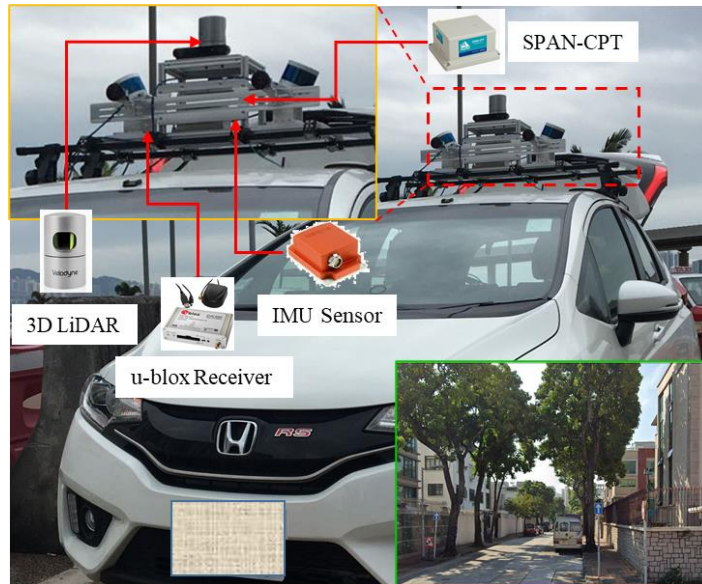


Fig. 3. Illustration of the data collection vehicle and tested scenarios.

We analyzed the performance of GNSS-RTK positioning by comparing several methods, as shown below. The objective of this analysis was to validate the effectiveness of the proposed method in improving the GNSS-RTK positioning. The accuracy is evaluated in the ENU frame by selecting the first point as the reference position.

- (a) **GNSS-RTK:** conventional GNSS-RTK positioning solution [23] via the raw measurements from the u-blox M8T receiver. Meanwhile, the ambiguity is solved by an epoch-by-epoch basis.
- (b) **u-blox:** commercial GNSS positioning solution output from the u-blox M8T receiver, without the correction from the reference stations.
- (c) **GNSS-RTK-C:** GNSS-RTK positioning solution aided by GNSS NLOS exclusion using the proposed method, via the raw measurements from the u-blox M8T receiver. Meanwhile, the ambiguity is solved by an epoch-by-epoch basis.

Be noted that we directly evaluate the performance of the GNSS-RTK positioning, therefore showing the effectiveness of the proposed method.

6.2 Performance Evaluation in Urban Canyon

The results of the above-mentioned three methods are shown in Table 1. The first row shows the number of satellites being used in the positioning estimation. A mean number of 17 satellites are received for GNSS positioning. After applying the proposed GNSS NLOS exclusion, the mean number of satellites decreases to 15.8. The second column shows the 2D positioning error of the u-blox receiver. The positioning result is based on standard NMEA [27] messages from the u-blox receiver. A mean error of 6.25 meters was obtained, with a standard deviation of 7.31 meters. The maximum error reached 38.53 meters. The GNSS solution was available throughout the experiment. The third column shows the conventional GNSS-RTK positioning result. The mean error decreases to 2.43 meters after using both the raw measurements from the u-blox receiver and the reference station. The standard deviation (STD) and the maximum error decrease to 1.16 meters and 7.20 meters, respectively. We can see that the fixed rate is only 1.0% due to the poor measurement quality. With the help of the proposed method by excluding the GNSS NLOS measurements, the mean error decreases to 1.95 meters with a standard deviation of 1.003 meters. However, the maximum error increases from 7.20 (GNSS-RTK) to 12.40 meters (GNSS-RTK-C). Fortunately, the fixed rate increases slightly to 1.6% after excluding the NLOS receptions. The improved GNSS positioning results demonstrate the effectiveness of the proposed method in mitigating the effects of NLOS signals.

The trajectories of the evaluated three methods together with the ground truth are shown in Fig. 4. The positioning errors throughout the experiment are shown in Fig. 5. Interestingly, we can see that near epoch A annotated by a circle in Fig. 5, the

positioning error arising from the proposed method is significantly larger than the conventional GNSS-RTK which is due to the excessive exclusion of the GNSS NLOS. The scene near epoch A is shown in the middle of Fig. 4 which involves dense foliage. The bottom panel of Fig. 5 shows the number of satellites being excluded. 4 satellites are detected as NLOS using the generated point cloud map. As a result, the geometry of the satellite distribution is significantly distorted leading to increased positioning error. A similar phenomenon was also found in our previous work [4, 28, 29].

Table 1. Positioning performance comparison.

Items	u-blox	GNSS-RTK	GNSS-RTK-C
Mean satellite number	17	17	15.8
Mean error	6.25 m	2.43 m	1.95 m
STD	7.31 m	1.16 m	1.003 m
Maximum error	38.53 m	7.20 m	12.40 m
Fixed-rate		1.0%	1.6 %

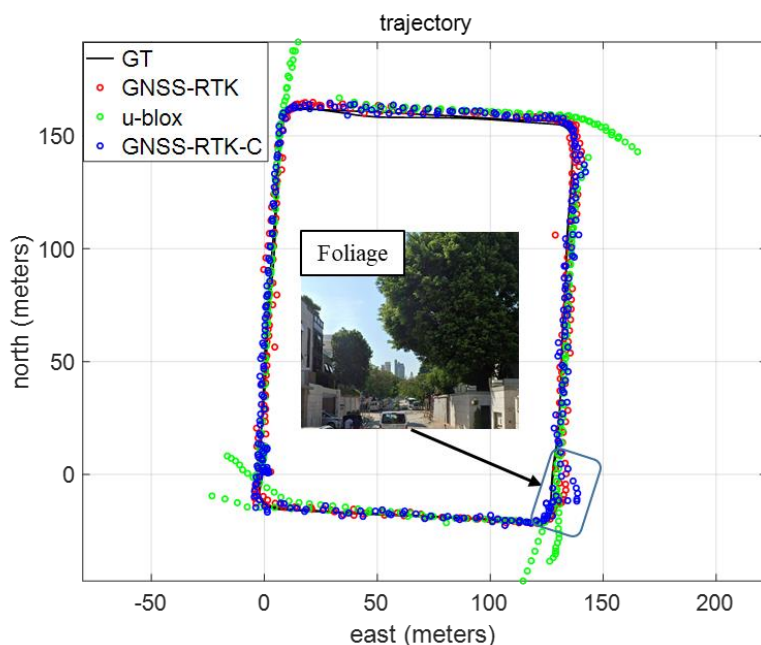


Fig. 4. Trajectories of the evaluated methods. The black curve denotes the ground truth (GT). The red, green, and blue curves denote the solutions from GNSS-RTK, u-blox, and GNSS-RTK-C, respectively.

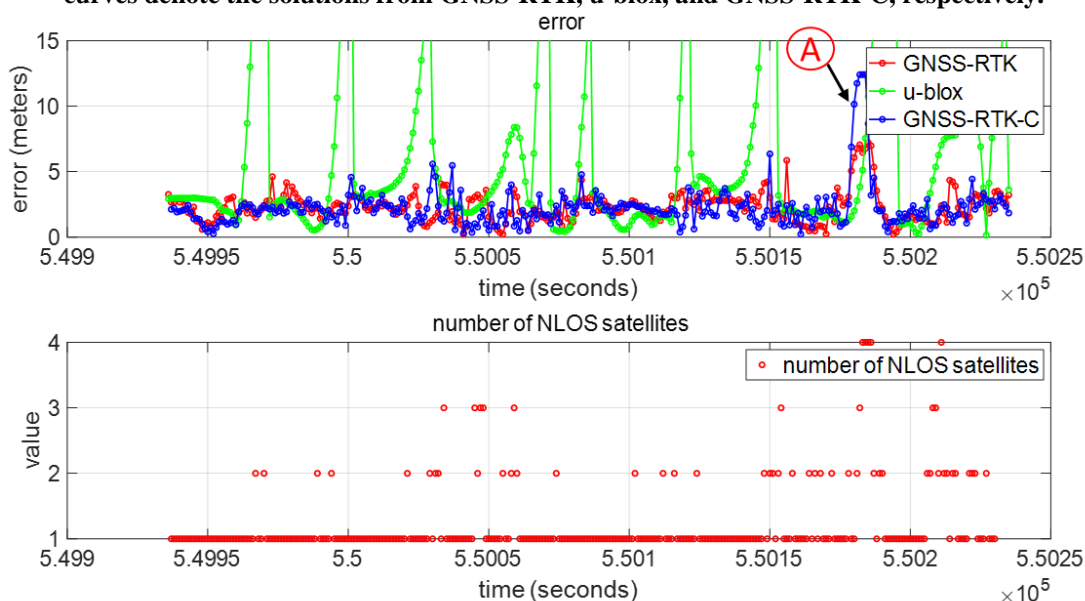


Fig. 5. The top panel shows the errors of the evaluated methods. The red, green, and blue curves denote the solutions from GNSS-RTK, u-blox, and GNSS-RTK-C, respectively. The bottom panel shows the number of excluded GNSS NLOS satellites during the experiment.

In short, the proposed method (GNSS-RTK-C) effectively detects and excludes the potential GNSS NLOS leading to improved performance, compared with the conventional method (GNSS-RTK). However, the fixed rate is still limited at 1.0% for GNSS-RTK and 1.6% for GNSS-RTK-C. The major problem is caused by the poor geometry of the satellite distribution due to the proposed GNSS NLOS exclusion.

6. CONCLUSIONS AND FUTURE WORK

GNSS-RTK positioning is currently still the indispensable source for autonomous driving localization which requires accurate and absolute positioning. Unfortunately, the application of GNSS-RTK positioning in the urban canyon is still limited due to the signal reflection and poor satellite geometry. This paper opens a new window for improving the GNSS-RTK by detecting and excluding the potential GNSS NLOS using onboard sensing (LiDAR/inertial integration). The accuracy of the GNSS-RTK is improved from 2.43 to 1.95 meters in the evaluated dataset with the help of the proposed NLOS exclusion. Overall, we believe that the proposed method can have a positive impact on both the academic and industrial fields.

According to the results, the fixed rate of GNSS-RTK is still limited in the evaluated dataset due to the poor satellite geometry after the GNSS NLOS exclusion. In the future, we will explore using the perceived environmental features to improve the geometry constraint to further increase the fixed rate of the GNSS-RTK in urban canyons. Moreover, the generated PCM is still limited by the field of view of the onboard 3D LiDAR. In the future, we will employ multiple 3D LiDARs to improve the FOV of the environment reconstruction.

REFERENCES

- [1] P. J. Teunissen and A. Kleusberg, *GPS for Geodesy*. Springer Science & Business Media, 2012.
- [2] G. Wan *et al.*, "Robust and precise vehicle localization based on multi-sensor fusion in diverse city scenes," in *2018 IEEE International Conference on Robotics and Automation (ICRA)*, 2018: IEEE, pp. 4670-4677.
- [3] P. J. Teunissen, "Least-squares estimation of the integer GPS ambiguities," in *Invited lecture, section IV theory and methodology, IAG general meeting, Beijing, China*, 1993.
- [4] W. Wen, G. Zhang, and L. T. Hsu, "Correcting NLOS by 3D LiDAR and building height to improve GNSS single point positioning," *Navigation*, vol. 66, no. 4, pp. 705-718, 2019, doi: <https://doi.org/10.1002/navi.335>.
- [5] R. Furukawa, N. Kubo, and A. El-Mowafy, "Prediction of RTK-GNSS Performance in Urban Environments Using a 3D model and Continuous LoS Method," in *Proceedings of the 2020 International Technical Meeting of The Institute of Navigation*, 2020, pp. 763-771.
- [6] P. Fan, W. Li, X. Cui, and M. Lu, "Precise and robust RTK-GNSS positioning in urban environments with dual-antenna configuration," *Sensors*, vol. 19, no. 16, p. 3586, 2019.
- [7] T. Li, H. Zhang, Z. Gao, Q. Chen, and X. Niu, "High-accuracy positioning in urban environments using single-frequency multi-GNSS RTK/MEMS-IMU integration," *Remote sensing*, vol. 10, no. 2, p. 205, 2018.
- [8] G. C. Chung, S. T. Su, and M. Y. Alias, "Adaptive Windowed Statistical Selection Rake for Long Ultra-Wideband Multipath Channels," (in English), *Wireless Pers Commun*, vol. 98, no. 1, pp. 453-466, Jan 2018, doi: 10.1007/s11277-017-4878-8.
- [9] H. T. Zhang, "Performance Comparison of Kinematic GPS Integrated with Different Tactical Grade IMUs," *CALGARY, ALBERTA: THE UNIVERSITY OF CALGARY*, 2006.
- [10] P. Henkel, A. Blum, and C. Günther, "Precise RTK Positioning with GNSS, INS, Barometer and Vision," in *Proceedings of the 30th International Technical Meeting of the Satellite Division of The Institute of Navigation (ION GNSS+ 2017)*, 2017, pp. 2290-2303.
- [11] T. Li, H. Zhang, Z. Gao, X. Niu, and N. El-Sheimy, "Tight fusion of a monocular camera, MEMS-IMU, and single-frequency multi-GNSS RTK for precise navigation in GNSS-challenged environments," *Remote Sensing*, vol. 11, no. 6, p. 610, 2019.
- [12] X. B. W. Wen and L.-T. Hsu, "Performance analysis of visual/inertial integrated positioning in typical urban scenarios of Hong Kong," 2019.
- [13] W. Wen, G. Zhang, and L.-T. Hsu, "GNSS NLOS exclusion based on dynamic object detection using LiDAR point cloud," *IEEE Transactions on Intelligent Transportation Systems*, 2019.
- [14] G. Z. Weisong Wen, Li-ta Hsu, "Correcting GNSS NLOS by 3D LiDAR and Building Height," presented at the ION GNSS+, 2018, Miami, Florida, USA., 2018.

- [15] W. Wen, G. Zhang, and L.-T. Hsu, "Exclusion of GNSS NLOS receptions caused by dynamic objects in heavy traffic urban scenarios using real-time 3D point cloud: An approach without 3D maps," in *Position, Location and Navigation Symposium (PLANS), 2018 IEEE/ION*, 2018: IEEE, pp. 158-165.
- [16] W. Wen, "3D LiDAR Aided GNSS and Its Tightly Coupled Integration with INS Via Factor Graph Optimization," in *Proceedings of the 33rd International Technical Meeting of the Satellite Division of The Institute of Navigation (ION GNSS+ 2020)*, 2020, pp. 1649-1672.
- [17] J. Zhang, W. Wen, F. Huang, X. Chen, and L.-T. Hsu, "Coarse-to-Fine Loosely-Coupled LiDAR-Inertial Odometry for Urban Positioning and Mapping," *Remote Sens-Basel*, vol. 13, no. 12, p. 2371, 2021.
- [18] W. Wen, G. Zhang, and L.-T. Hsu, "Object-Detection-Aided GNSS and Its Integration With Lidar in Highly Urbanized Areas," *IEEE Intelligent Transportation Systems Magazine*, vol. 12, no. 3, pp. 53-69, 2020.
- [19] Z. Zhang, "Parameter estimation techniques: A tutorial with application to conic fitting," *Image vision Computing*, vol. 15, no. 1, pp. 59-76, 1997.
- [20] S. Agarwal and K. Mierle. "Ceres Solver." <http://ceres-solver.org> (accessed 6 January 2021).
- [21] J. J. Moré, "The Levenberg-Marquardt algorithm: implementation and theory," in *Numerical analysis*: Springer, 1978, pp. 105-116.
- [22] E. Kaplan and C. Hegarty, *Understanding GPS: principles and applications*. Artech house, 2005.
- [23] T. Takasu and A. Yasuda, "Development of the low-cost RTK-GPS receiver with an open source program package RTKLIB," in *International symposium on GPS/GNSS*, 2009: International Convention Center Jeju Korea, pp. 4-6.
- [24] W. Wen and L.-T. Hsu, "Towards Robust GNSS Positioning and Real-time Kinematic Using Factor Graph Optimization," *arXiv preprint arXiv:2106.01594*, 2021.
- [25] P. Teunissen, "Theory of integer equivariant estimation with application to GNSS," *Journal of Geodesy*, vol. 77, no. 7-8, pp. 402-410, 2003.
- [26] M. Quigley *et al.*, "ROS: an open-source Robot Operating System," in *ICRA workshop on open source software*, 2009, vol. 3, no. 3.2: Kobe, Japan, p. 5, doi: <http://www.cim.mcgill.ca/~dudek/417/Papers/quigley-icra2009-ros.pdf>.
- [27] P. D. Groves, *Principles of GNSS, inertial, and multisensor integrated navigation systems*. Artech house, 2013.
- [28] W. X., W., Zhang, G., Hsu, Li-Ta, "Real-time GNSS NLOS Detection and Correction Aided by Sky-Pointing Camera and 3D LiDAR," presented at the Proceedings of ION Pacific PNT 2019, Honolulu, HA, USA, 2019.
- [29] X. Bai, W. Wen, and L.-T. Hsu, "Using Sky-pointing fish-eye camera and LiDAR to aid GNSS single-point positioning in urban canyons," *IET Intelligent Transport Systems*, vol. 14, no. 8, pp. 908-914, 2020.